Acta Geod Geophys (2015) 50:403–417
DOI 10.1007/s40328-015-0110-z

# Mantle plume characteristics in three-dimensional depth- and temperature-dependent models

**Bálint Süle**[1]

Received: 31 October 2014 / Accepted: 16 March 2015 / Published online: 4 April 2015


**Abstract** Numerical calculations in three-dimensional Cartesian geometry have been carried out. The aim of the paper is to investigate systematically the effect of Rayleigh number and temperature- and depth-dependent viscosity on the radius and temperature anomaly of mantle plumes and on surface observable characteristics like topography and geoid anomaly. As reference models depth-dependent models were chosen, then the addition of weak and stronger temperature-dependence was studied. The Rayleigh number changed between $10^5$ and $10^7$. If viscosity decreases with temperature the convection becomes more vigorous and thermally weaker plumes rise from the bottom boundary layer. The radius and temperature anomaly of the upwelling decreases with increasing temperature-dependence. Topographic uplift significantly decreases with increasing temperature-dependence. For weak depth-dependent models the geoid decreases together with the topography as Rayleigh number increases. However, strongly depth-depend models show negative geod anomaly above the hot plume. In case of temperature- and depth dependent models the geoid have a maximum in the function of Rayleigh number. This maximum appears at different Rayleigh number depending on the actual factors of temperature- and depth-dependence. The amplitudes of topographic uplift in the case of stronger temperature-dependence and high Rayleigh number are not far from the observed values, but the geoid signal is higher by a factor of about 2.

**Keywords** Mantle plumes · Mantle convection · Dynamic topography · Geoid

✉ Bálint Süle
suba@seismology.hu

[1] Kövesligethy Radó Seismological Observatory, MTA CSFK GGI, Meredek u. 18, Budapest 1112, Hungary

## 1 Introduction

The motion of lithosphere plates suggests a large convective system in the Earth's mantle. During the thermal convection the hot, light material ascends and the cold, heavy one descends. The downwellings in the mantle are located at the subduction zones, where lithosphere plates sink into the deep. It would be obvious that similarly sheet-like upwellings could be found at mid-ocean ridges. But nowadays it has been commonly assumed that upwellings beneath mid-ocean ridges are only passive responses to the diverging plates by the pull of sinking slabs. Seismic tomographic images clearly indicate the presence of seismically low (i.e. hot) regions beneath ridges, but these anomalies do not extend deeply into the mantle (Woodhouse and Dziewonski 1984; Su et al. 1992). On the other hand ridges have a negligible geoid signature (i.e. they are isostatically compensated) and their topography can be explained by the cooling of the lithosphere (Davies 2000). Since the pioneering work of Morgan (1971) it is widely accepted that the main upwellings of mantle convection have relatively thin cylindrical shape (mantle plumes) and are located beneath the hotspots (Bercovici et al. 1989). Hotspots are anomalous areas of surface volcanism associated with topographic swells and positive geoid anomalies.

Recent results from seismic tomography support the existence of mantle plumes. Different tomographic methods showed negative seismic anomalies beneath individual hotspots (Wolfe et al. 1997; Ji and Nataf 1998; Bijwaard and Spakman 1999). Finite-frequency tomographic images presented evidence for plumes arising from the lowermost mantle (Montelli et al. 2004, 2006).

Early hotpsot models (Crough 1978; Detrick and Crough 1978) did not take into account the dynamical processes in the formation of swells but focused on the thermal structure of the lithosphere. Nowadays, it has been commonly assumed that the best theoretical model of hotspot swells is the mantle plume model. A number of papers have analyzed the topographic and geoid signal of mantle plumes either in 2D Cartesian (Robinson and Parsons 1988) or in 2D axy-symmetric models (King 1997; Shahraki and Schmeling 2012) investigating the effect of stratified (Robinson and Parsons 1988) or temperature- and pressure-dependent viscosity (Shahraki and Schmeling 2012). Süle (2005) studied the topographic and geoid anomalies of plumes in 3D Cartesian geometry assuming depth-dependent, stratified viscosity. 3D modeling of plume–lithosphere interaction successfully explained the geoid-to-topography ratio at the Hawaiian swell (Cserepes et al. 2000).

This paper studies systematically the effect of the Rayleigh number and the temperature- and depth- dependent viscosity on the most important observable characteristics of plumes: size, temperature anomaly, topographic and geoid height.

## 2 Model description

The calculations have been carried out in 3D Cartesian domain. The thermal convection is described by the equation of continuity, the Navier–Stokes equation and the heat transport equation. Boussinesq approximation was used in the following non-dimensional form, respectively (Albers 2000):

$$\nabla \cdot \mathbf{v} = 0 \tag{1}$$

$$-\nabla p + \nabla \cdot \left(\eta(\nabla \mathbf{v} + (\nabla \mathbf{v})^T)\right) + RaT\mathbf{e}_z = 0 \tag{2}$$

$$\frac{\partial T}{\partial t} + \nabla \cdot (\mathbf{v}T) = \nabla^2 T \tag{3}$$

where $\mathbf{v} = (u, v, w)$ means velocity, $p$ the nonhydrostatic pressure component, $\eta$ dynamic viscosity, $T$ temperature, $\mathbf{e}_z$ unit vector antiparallel to the direction of gravity and $t$ time. $Ra$ is the Rayleigh number, which is the ratio of buoyancy force and viscous force and defined by

$$Ra = \frac{\rho_0 \alpha \Delta T d^3}{\kappa \eta_0} \tag{4}$$

with $\alpha$ thermal expansivity, $g$ gravitational acceleration, $\Delta T$ temperature drop across the box, $d$ thickness of the layer, $\kappa$ thermal diffusivity, $\rho_0$ and $\eta_0$ reference values of density and viscosity. Equations (1)–(3) were solved with a second-order finite-volume discretization in combination with a multigrid method (Albers 2000).

The aim of this paper is to study the effect of the temperature-dependence of the viscosity in addition to the depth-dependence, hence the following viscosity law was applied:

$$\eta(z, T) = exp[ln(\delta)z - ln(\tau)T] \tag{5}$$

where the non-dimensional viscosity depends exponentially on the non-dimensional depth $z$ and temperature $T$. The scaling factors $\delta$ and $\tau$ represent the viscosity contrast caused by the depth and temperature, respectively. For example, if $\delta = 10$ and $\tau = 100$ is assumed, the viscosity increases from 1 to 10 from to top to the bottom and decreases two orders of magnitude as the temperature increases from 0 to 1.

Various kinds of inversion models (Čadek and van den Berg 1998; King and Masters 1992; Mitrovica and Forte 1997) show that viscosity increases 1–2 orders of magnitude from the upper to the lower mantle due to the pressure. Numerical simulations suggest that the depth dependence of viscosity has large effect on the global pattern of mantle convection (Cserepes 1993; Tackley 1996). Sheet-like downwellings and cylindrical

**Table 1** The horizontal aspect ratio of the model box in the investigated models

| $\delta$ | $\tau$ | $Ra$ | | | | |
|---|---|---|---|---|---|---|
| | | 1e5 | 5e5 | 1e6 | 5e6 | 1e7 |
| 5 | 0 | 2 | 1.5 | 1.0 | 1 | 0.7 |
| | 2 | 1 | 0.7 | 0.5 | 0.3 | 0.3 |
| | 5 | 1 | 0.5 | 0.4 | 0.3 | 0.3 |
| | 10 | 0.8 | 0.5 | 0.4 | 0.3 | 0.3 |
| 10 | 0 | 2 | 1.5 | 1.5 | 1 | 0.7 |
| | 2 | 1.5 | 1 | 1 | 0.7 | 0.7 |
| | 10 | 1 | 1 | 1 | 0.7 | 0.5 |
| | 100 | 1 | 0.5 | 0.4 | 0.4 | 0.4 |
| 100 | 0 | 2.5 | 2 | 2 | 1.5 | 1.2 |
| | 2 | 1.5 | 1 | 1 | 1 | 1 |
| | 10 | 1.5 | 1 | 1 | 1 | 1 |
| | 100 | 1 | 1 | 1 | 0.5 | 0.4 |

upwellings characterize the convection in case of increasing viscosity with depth. In this study depth-dependent models as reference models were chosen with values of $\delta = 5, 10$ and 100. In order to study systematically the effect of the addition of the temperature-dependence, three scaling factors $\tau$ have been applied beside one given $\delta$. The Rayleigh number changed from $10^5$ to $10^7$ for all viscosity function. The applied combinations of $\delta$ and $\tau$ together with the Rayleigh numbers can be found in Table 1.

Both the upper and the lower boundaries of the model box were supposed to be isothermal and stress-free. On the sidewalls mirror symmetry was prescribed. The iteration was started from conductive initial condition with a small perturbation of the temperature in one corner of the box. The size of the box was chosen to allow the evolution of only one plume in one corner of the box to eliminate the interaction of different plumes in the geoid and topography. According to the mentioned boundary conditions the model domain represents one quarter of the whole convective cell (Fig. 1). The horizontal size of the convective cell strongly depends on the physical conditions. The applied horizontal dimensions of the model box are given in Table 1. In cases without temperature-dependence the box size agrees well with the results of Galsa and Cserepes (2003). Although at such high Rayleigh numbers one could expect time-dependent convection, in case of such small boxes steady state convection can evolve. All of the following results characterize steady state solutions.

Topographic uplift can be calculated by equating the surface normal stress $\sigma_{zz}$ to the buoyancy (per unit area) of the topography. Thus, the topography $h$ of an interface between two medium with density contrast $\Delta\rho$ is given by the equation:

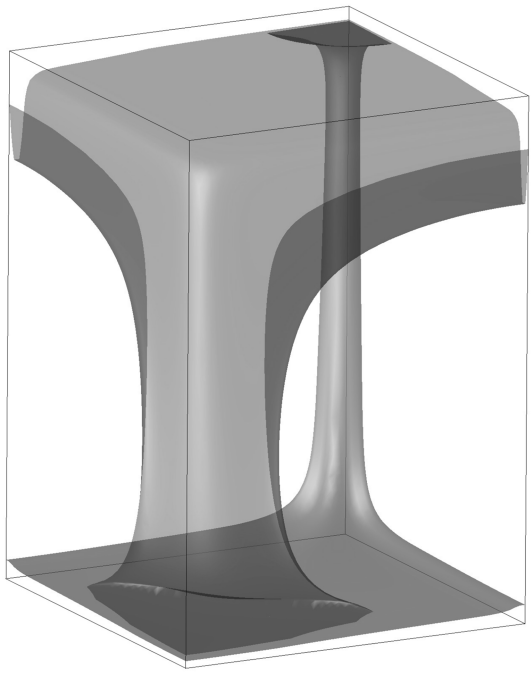

**Fig. 1** Isothermic surface of $T = 0.6$ (*red* denotes hot plume in one corner) and $T = 0.25$ (*blue* is cold downwelling in the opposite corner). Model parameters are $\delta = 10$, $\tau = 10$ and $Ra = 5 \times 10^5$. (Color figure online)

$$h = \frac{\sigma_{zz}}{\Delta\rho g} \tag{6}$$

Overlying water was supposed (oceanic hotspots) above the upper boundary. Geoid anomalies were calculated by summing the gravitational effects of three components: two terms associated with the mass anomalies of the surface and bottom topography and one term is due to the internal density distribution caused by thermal expansion. For calculating these anomalies we need some dimensional physical units, which are summarized in Table 2. Topography and geoid anomalies were normalized by setting their mean to zero. For verification of the calculation method of surface anomalies at the applied numerical resolution benchmark calculations have been done. The results agree well with the values of the benchmark study of Busse et al. (1993).

## 3 Results

### 3.1 Thermal structure

Although this paper focuses on the plume individual characteristics, it is worthy to talk about the global structure of convection. If the Rayleigh number is higher then the critical value, heat is transported also by the form of convection. Increasing Rayleigh number results in more vigorous convection with a boundary layer structure. At high Rayleigh numbers thermal boundary layers are formed at the top and bottom of the fluid layer. The vertical temperature gradient in these layers is high, while the inside of the convective cell is isothermal (Fig. 2). In isoviscous fluid the upwellings and downwellings are symmetrical, the average temperature inside the box is about $T = 0.5$. Assuming increasing viscosity with depth cylindrical upwellings and sheet-like elongated downwellings evolve (Cserepes 1993). In the higher viscosity provinces the convection slows down, hence the velocity decreases in the bottom layer and heat flux reduces. Because of the reduced heat flux income the average temperature of the convective cell decreases. The higher viscosity difference between the bottom and the top causes lower inner temperature. Figure 2 illustrates this situation in our base models without temperature-dependence ($\delta = 10, 100$ and $\tau = 0$).

The addition of temperature-dependence results in a three-dimensional viscosity distribution having the similar boundary layer structure as the temperature (Fig. 3). In the upper boundary layer the temperature increases rapidly with depth. Thus, the viscosity decreases quickly downwards. Beneath the top boundary layer, in the inner part of the convective cell the temperature is constant, hence the depth-dependence dominates and the viscosity increases to a maximum value above the bottom boundary layer. Approaching the bottom the temperature gradient again turns up leading to rapidly decreasing viscosity. The viscosity profile of Earth's mantle has similar structure: bellow the surface the high

**Table 2** Physical parameters for calculating the topographic and geoid anomalies

| $d$ | $\alpha\Delta T$ | $\rho_{mantle}$ | $\rho_{core}$ | $\rho_{water}$ |
|---|---|---|---|---|
| $2.9 \times 10^6$ m | $5.0 \times 10^{-2}$ | 4000 kg/m$^3$ | 8000 kg/m$^3$ | 1000 kg/m$^3$ |

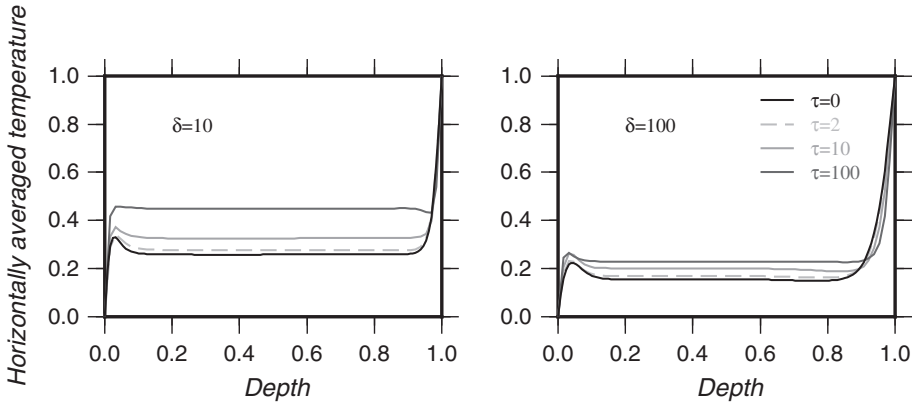


**Fig. 2** Effect of various temperature-dependent viscosity on the horizontally averaged temperature profile at depth-dependent viscosity of $\delta = 10$ (*left*) and $\delta = 100$ (*right*). $Ra = 10^7$ in all models

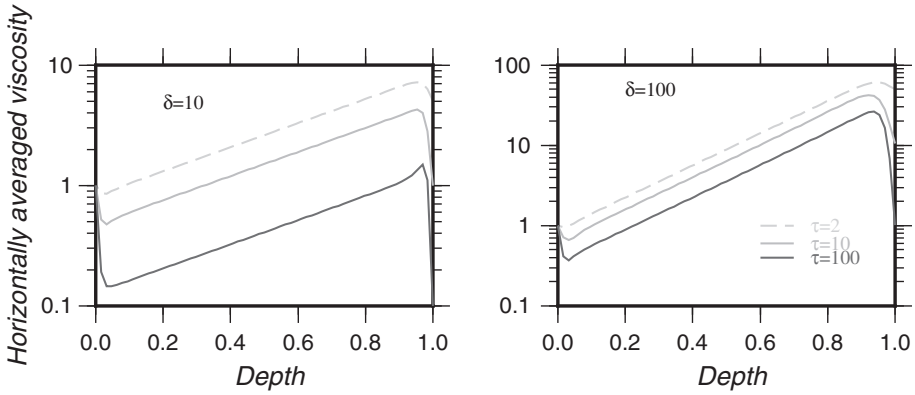


**Fig. 3** Horizontally averaged viscosity as the function of depth in cases of $\delta = 10$ (*left*) and $\delta = 100$ (*right*) with various strength of temperature-dependence ($\tau = 2, 10, 100$), at $Ra = 10^7$

viscosity lithosphere is followed by the low viscosity asthenosphere; then viscosity increases until the low viscosity layer of D″ at the core-mantle boundary.

Temperature-dependence has an opposite effect on the average temperature than the depth-dependence. Low viscosity in the hot bottom boundary layer induces faster convection and hence the increasing heat flux heats up the interior of the cell. The stronger temperature-dependence results in higher temperature of the internal region (Fig. 2).

A plume can be characterized by its size and temperature anomaly. For easy and consequent quantifying of these parameters the automatic plume detecting method of Galsa and Lenkey (2007) has been applied. The horizontal temperature distribution at a given depth was used to identify and quantify plumes. Grid points where the temperature is higher than a threshold value were regarded as the interior of a plume. The threshold temperature $T_{th}(z)$ was calculated from the horizontal average of temperature $T_{av}(z)$ and the maximum temperature $T_{max}(z)$ at the given depth:

$$T_{th}(z) = 0.45 \cdot (T_{max}(z) - T_{av}(z)) + T_{av}(z) \quad (7)$$

The isosurface of the threshold temperature defined the boundary of the plume. The plume radius was calculated as the average distance between the locations of the maximum and the threshold temperature. The excess temperature of the plume was computed as the difference between the average plume temperature and the average temperature of the plain ($T_{av}$). Figure 4 summarizes the radius and temperature anomalies of plumes in the 60 model calculations at the half depth ($z = 0.5$) of the box.

The upwelling starts from the bottom boundary layer forming a narrow, cylindrical column and expands beneath the top boundary (Fig. 1). In lower viscosity regions the flow

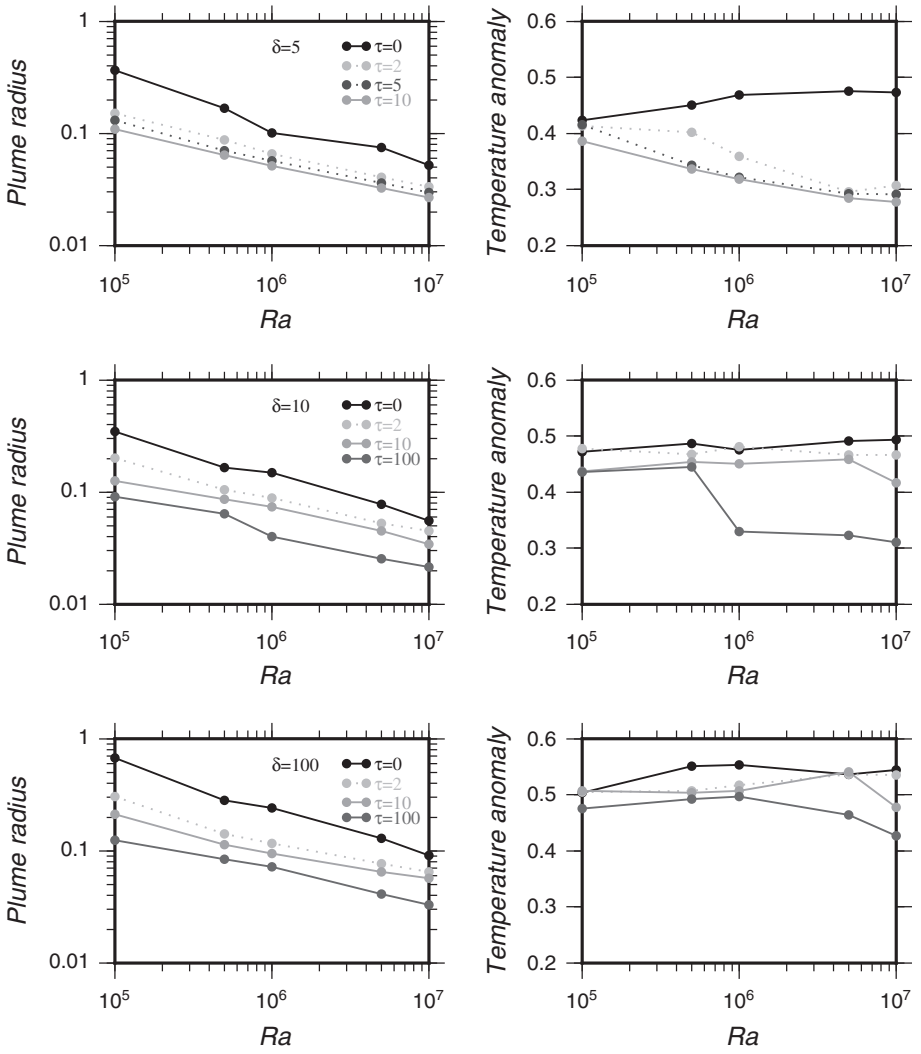


**Fig. 4** Plume radius (*left*) and average temperature anomaly of the plume (*right*) as the function of Rayleigh number at the half depth of the box. $\delta$ and $\tau$ values are shown in the *left side* figures

accelerates and narrower plume can maintain the same mass flux, while plumes in the deep have thick roots, specially in strongly depth dependent models (e.g. Fig. 5).

Increasing Rayleigh number leads to thinner boundary layers and plumes become narrower. In isoviscous fluid the radius decrease with approximately 1/3 power of Rayleigh number (Galsa and Lenkey 2007). This relation does not change significantly by adding either depth- or depth- and temperature-dependent viscosity (Fig. 4). At given depth the stronger depth-dependence (larger $\delta$) leads to wider diameter as mentioned above. The addition of temperature-dependence produces narrower upwellings. Increasing $\tau$ reduces the viscosity in the hot plumes, convection accelerates and upwellings become thinner. Stronger temperature-dependence decreases the radius in the similar way in all of the models (Fig. 4), that suggest a power-law relation between the plume radius and $\tau$.

In isoviscous fluid the average horizontal temperature and the plume temperature at the half depth are about 0.5 and 0.8, respectively and are insensitive to the Rayleigh number (Galsa and Lenkey 2007). If the viscosity increases with depth the average temperature is reduced as was mentioned above. On the other hand the temperature of the plume does not change significantly, hence the anomaly increases with $\delta$. Changing the Rayleigh number does not have great influence on the temperature anomaly of the plume neither in depth-dependent models (Fig. 4).

The addition of weak temperature-dependence to strong depth-dependent models results in slightly increased average temperature (see in Fig. 2 the $\delta = 100$ cases), hence the anomaly becomes a little smaller (Fig. 4). In weakly depth-dependent models the addition of temperature-dependence leads to stronger decrease of anomaly. In these cases, when

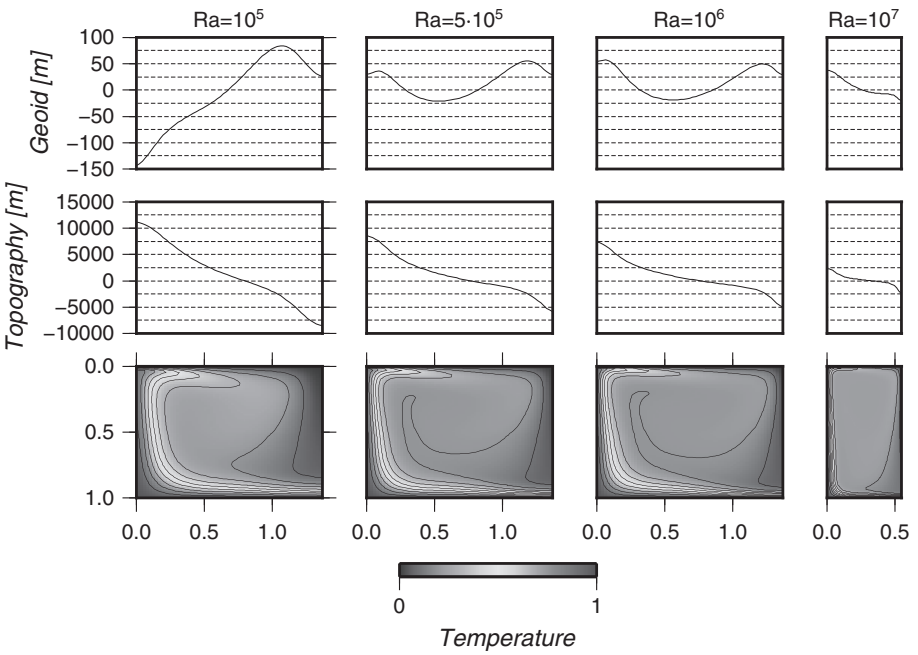


**Fig. 5** Effect of the Rayleigh number on the geoid (*upper row*), the topography (*middle row*) and temperature field (*lower row*) in the diagonal cross section of the box. Scaling factors of the viscosity $\delta = \tau = 100$, temperature isocontours are $T = 0.1, 0.2, \ldots, 0.9$. Aspect ratio of the model domain varies with *Ra* (see Table 1)

temperature-dependence dominates, the anomaly of plume depends on the Rayleigh number. In the $\delta = 5$ models yet at lower Rayleigh numbers the anomaly decreases strongly in all temperature-dependent cases. Assuming $\delta = 10$ and $\tau \leq 10$ the anomaly is lower than in the only depth-dependent case, but does not change notably with Rayleigh number. The dependence on Rayleigh number appears if $\tau = 100$ is supposed (Fig. 4). In the cases of $\delta = 100$ models this dependence can not observed clearly since the applied factors of $\tau =$ are in the same order of magnitude as $\delta$.

### 3.2 Topography and geoid

Thermal structure of plumes has been analyzed by non-dimensional quantities, as usual in fluid dynamics. However, in the case of observable surface manifestations of mantle convection like the topography and the geoid it is worthy to work with the dimensional values for comparison with observation. On the other hand in calculation of topography and geoid the Earth's gravitational acceleration and density of the mantle was used, which indicates that the following analyses can be interpreted in the context of Earth. For these reasons the dimensional forms will be presented.

Examples of profiles of topographic and geoid anomalies can be seen in Figs. 5, 6 and 7. In Fig. 5 the effect of the increasing Rayleigh number is shown, while Figs. 6 and 7

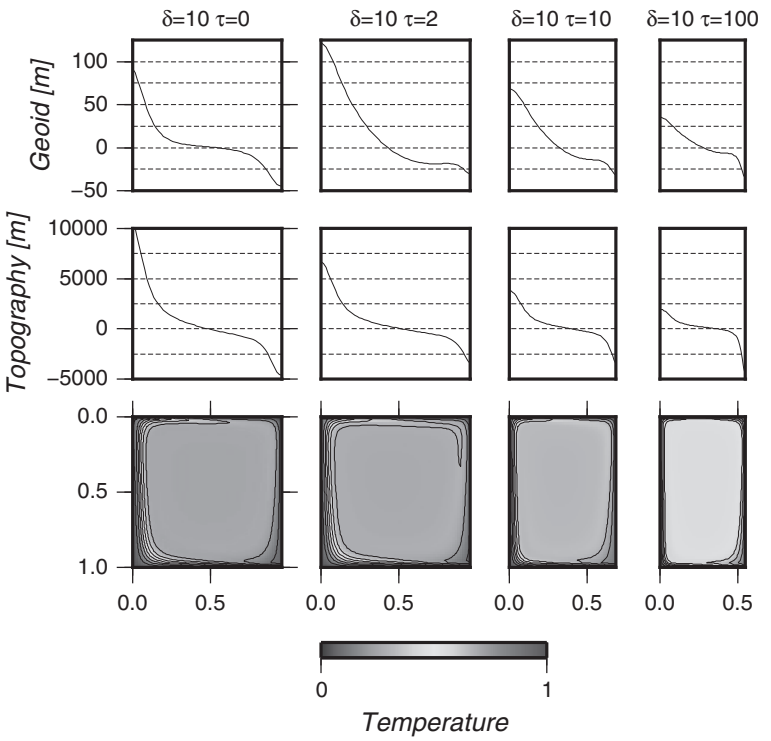


**Fig. 6** Effect of the temperature-dependence on the geoid (*upper row*), the topography (*middle row*) and and temperature field (*lower row*) in the diagonal cross section of the box. At depth-dependent viscosity $\delta = 10$ and $Ra = 10^7$. Temperature isocontours are $T = 0.1, 0.2, \ldots, 0.9$. Aspect ratio of the model domain varies with *Ra* (see Table 1)

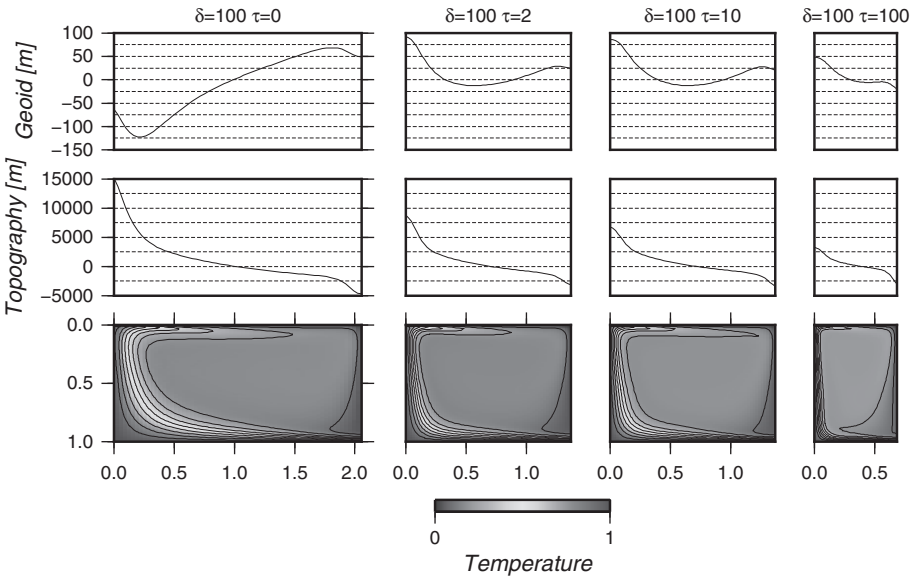


**Fig. 7** Effect of the temperature-dependence on the geoid (*upper row*), the topography (*middle row*) and and temperature field (*lower row*) in the diagonal cross section of the box. At depth-dependent viscosity $\delta = 100$ and $Ra = 5 \times 10^5$. Temperature isocontours are $T = 0.1, 0.2, \ldots, 0.9$

demonstrate the effect of increasing temperature-dependence. Figure 8 shows the peak topographic and geoid anomalies induced by the plume in the various models.

Topography was calculated using Eq. (6). During the numerical simulation physical quantities are treated in non-dimensional form. Dimensionless normal stress $\sigma'_{zz}$ can be converted to dimensional units by multiplying by $\eta_0\kappa/d^2$. Applying the definition of the Rayleigh number (Eq. 4) dimensional surface topography can be determined by

$$h = \frac{\alpha \Delta T d \rho_0}{Ra} \frac{\sigma'_{zz}}{\Delta \rho} \tag{8}$$

Although $\sigma'_{zz}$ increases with increasing Rayleigh number, the dimensional topography decreases (Fig. 8). Since we use the same scaling factors of $\alpha T$, $d$, $\rho_0$ in case of every model calculation, the change of Rayleigh number can be imagined as varying $\eta_0$. If $\eta_0\kappa$ was fixed, Rayleigh number would be controlled by $\Delta T$. In case of mantle convection holding $\Delta T$ constant is preferred instead of $\eta_0$ (Kiefer and Hager 1992).

In $\tau = 0$ models the peak topographic anomalies are approximately the same (Fig. 8). Increasing viscosity with depth changes radically the temperature structure of the convection but has no significant effect on the surface deformation. It is readily understood due to the fact that increasing $\delta$ has effect on the bottom boundary layer and does not change the top region.

If temperature-dependence is added, the viscosity inside the hot plume decreases rapidly as a consequence of the excess temperature. The low viscosity can not maintain so high topography as in cases of $\tau = 0$. The uplift decreases with increasing $\tau$ because the stronger temperature-dependence lowers the viscosity and so the normal stress.

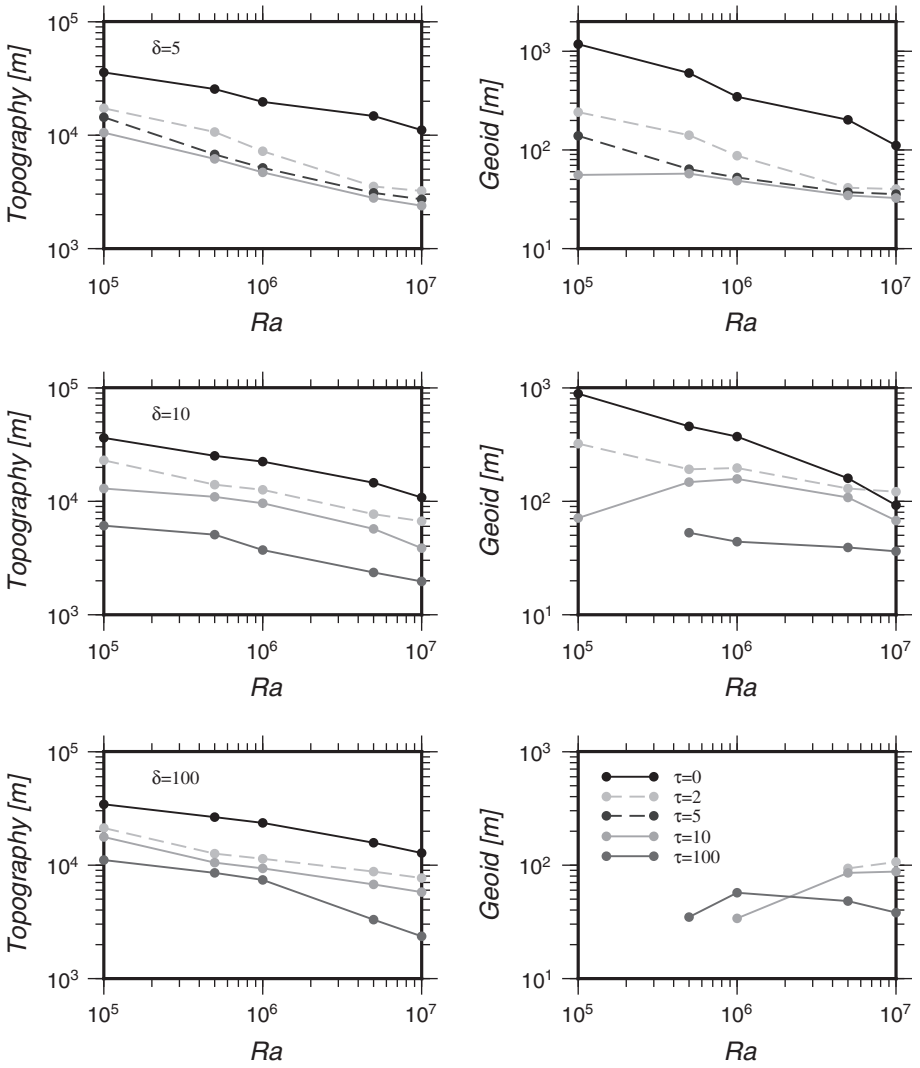


**Fig. 8** Peak topographic (*left*) and geoid (*right*) anomalies of plumes in the calculated models plotted against the Rayleigh number. Legend is inserted in the *bottom right* figure

Although this paper focuses on the plumes, it is worth looking at the topography above the center of downwellings. In case of depth-dependent models the absolute value of topography is much larger above the upwelling than above the downwelling. This difference decreases if increasing temperature-dependence is added (Figs. 5, 6, 7). If temperature-dependence dominates, the absolute value of the topography above the downwelling is the larger. In depth dependent models strong plumes dominate the convection. By adding temperature-dependence, plumes become weaker, which leads to lower relative topography.

Plume-induced geoid anomaly involves three effects: the gravitational effect of the bottom and top surface deformation and the gravitational effect of the internal density

structure caused by thermal expansion. The first two terms are positive, but the third contribution is negative due to the hot (and hence light) material of the upwelling. The sign of the geoid anomaly depends on the relative balance of the three terms. In isoviscous case the positive mass anomaly of the topography dominates [e.g. Kiefer and Hager (1992), King (1997)]. Weak depth-dependence does not change the sign of geoid anomaly, but supposing large $\delta$ the negative effect of the hot upwelling can dominate (Figs. 6, 7, $\tau = 0$ models). It is a consequence of that the topographic uplift does not change with increasing $\delta$, but the temperature anomaly of plume is influenced strongly by the depth-dependence. As mentioned in the previous section the internal of the convective cell cools down as $\delta$ increases and the temperature anomaly of the plume can be high enough the gravitational signal to dominate.

In Fig. 8 the peak geoid anomaly can be seen as the function of Rayleigh number at different values of viscosity scaling factors of $\delta$ and $\tau$, the negative anomalies of strongly depth-dependent models are not shown. If viscosity depends only on depth by a lower factor, the geoid decreases together with the topography as Rayleigh number increases (Fig. 8, $\tau = 0$ and $\delta = 5, 10$ models). The effect of Rayleigh number in depth- and temperature-dependent models is illustrated by Fig. 5. At low Rayleigh number $Ra = 10^5$ due to the strong depth-dependence $\delta = 100$ the negative gravitational anomaly dominates, which is caused by the hot material of the wide upwelling. As Rayleigh number increases, the topography decreases and the temperature anomaly of the plume does not change radically. One could thing that lower topography and the same excess temperature produces lower geoid, but in fact it is larger. Increasing Rayleigh number leads to narrower plume. The horizontal extent of topographic anomaly becomes smaller too, but with a smaller ratio. This way the interaction between the negative anomaly of the plume's hot mass and the positive anomaly caused by the broad topography forms the shape of geoid profile, which can be seen in Fig. 5 at $Ra = 5 \times 10^5$: a small deflection above the center of plume, then a local maximum is followed by the global minimum; towards the downwelling follows the global maximum and above the center of the downwelling a small deflection appears. As Rayleigh number increases, a positive geoid anomaly evolves above the plume (Fig. 5 , $Ra = 10^7$). It follows that the geoid will have a maximum as a function of Rayleigh number, as it is shown in Fig. 8. For example if $\delta = 10$ and $\tau = 10$, first the geoid increases from $Ra = 10^5$ to $Ra = 10^6$ and then decreases to higher Rayleigh numbers.

Figure 8 shows that in case of $\delta = 5$ the geoid anomalies are a much weaker function of $Ra$ when the temperature-dependence is stronger. For $\delta = 5$ and $\tau = 5$ peak geoid does not drop significantly as $Ra$ increases from $10^5$ to $10^7$. Moreover at these high Rayleigh numbers the obtained anomalies of $\tau = 2$ and $\tau = 5$ models are also very close to the value of the $\tau = 10$ model.

## 4 Discussion

Numerical simulations of mantle plumes in 3D Cartesian geometry have been carried out to study systematically the effect of the Rayleigh number and temperature- and depth-dependent viscosity on observable plume characteristics. The main goal of the paper is to analyze the effect of the mentioned parameters. Many important properties of mantle are not included in the model calculations, hence it is not expected that the results fully agree with the observations of real Earth.

If viscosity increases with depth the velocity decreases at the bottom boundary layer. The reduced income heat flux results in the decrease of the average temperature of the convective cell, thus the temperature anomaly of the plume becomes larger. Peak topography anomaly above the upwelling is not influenced strongly by increasing $\delta$, a huge uplift is located above the strong plume. Geoid signal of plume is dominated by the negative gravitational effect of the thick, hot mass of plume in case of strong depth-dependence.

Addition of temperature-dependent viscosity leads to low viscosity and high velocity in bottom boundary layer. As heat flux increases, the inner part of convective cell warms up and the temperature difference between the plume and the inner part of the cell is reduced. Upwellings of temperature-dependent models are thinner because of the increased velocity caused by the reduced viscosity. These remarks agree with the results of 2D cylindrical shell models of Kuslits et al. (2014). Topographic heights are much lower due to the low viscosity of plumes in temperature-dependent models. The relation between the Rayleigh number and the geoid anomaly strongly depends on the actual factor of temperature- and depth-dependence.

Seismic tomography studies (Wolfe et al. 1997; Ji and Nataf 1998; Bijwaard and Spakman 1999; Montelli et al. 2004, 2006) indicate at least 3–400 km radius and maximum 300 K temperature anomaly of plumes in the Earth's mantle. Hotpots swells typically rise to 1000–2000 m above the seafloor and are correlated with positive geoid anomalies of 1–12 m (Monnereau and Cazenave 1990; Sandwell and Mackenzie 1989; McNutt 1988; Crough 1978). In the model calculations presented in this study the plume radii change between 77 and 1740 km and temperature anomalies ranges from 780–1380 K (assuming whole mantle convection i.e. $d = 2900$ km and $\Delta T = 3000$ K temperature drop across the mantle). The peak topographic uplift varies from 36,117 to 1962 m and geoid anomalies (taking into account only the positive ones) are between 1185 and 34 m. The Rayleigh number of the mantle is in order of $10^7$, thus it is not surprising that models at $Ra = 10^7$ have the most realistic values. Generally speaking the modelled amplitude of the investigated anomalies are higher than the observed values, while their extent are smaller. The lowest excess temperature of plume appears in case of weak depth-dependence with stronger temperature-dependence ($\delta = 5$ and $\tau = 10$), but the plume radii are rather narrow in these models. In case of surface manifestations all of the models with $\delta = 100$ at the highest Rayleigh number has similar values: it can can be concluded that the depth- and temperature-dependent models at $Ra = 10^7$ have slightly higher topographic and 2–3 times larger geoid anomalies than geophysical observations.

Many important properties of mantle are not included in the presented model calculations. First of all viscosity can change many orders of magnitude due the temperature variations (Tackley 2000a, b). Regarding the presented tendencies this could have large effect on the anomalies. The other important thing is the heating mode of the convection. The Earth's mantle is not only basally heated from the core but mostly internally heated due to radioactive decay (Davies 2000). The addition of internal heating results in thermally weaker plume, hence both the excess temperature and the surface anomalies decrease (Süle 2005). Viscous stress, elastic deformation of lithosphere and deposited volcanic material also influence the topographic and geoid anomalies (Cserepes et al. 2000).

Previous 3D Cartesian study (Süle 2005) included depth-dependent, stratified viscosity models. Taking into account various viscosity layers (high viscosity lid—lithosphere, low viscosity asthenosphere and low viscosity D″ at core-mantle boundary) the temperature anomaly of plume can be lower than in the results of this paper. But in depth-dependent

models the topographic uplift is much higher than observed. Realistic swell high can not be predicted without temperature-dependent viscosity.

**Acknowledgments** This study was supported by the TAMOP-4.2.2.C–11/1/KONV-2012-0015 (Earth-system) project sponsored by the EU and European Social Foundation. The research was also supported by the Hungarian Scientific Research Fund (OTKA K-72665).

## References

Albers M (2000) A local mesh refinement multigrid method for 3-D convection problems with strongly variable viscosity. J Comput Phys 160:126–150

Bercovici D, Schubert G, Glatzmaier GA (1989) Three-dimensional spherical models of convection in the Earth's mantle. Science 244:950–955

Bijwaard H, Spakman W (1999) Tomographic evidence for a narrow whole mantle plume below Iceland. Earth Planet Sci Lett 166:121–126

Busse FH, Christensen U, Clever R, Cserepes L, Gable C, Giannandrea E, Guillou L, Houseman G, Nataf H-C, Ogawa M, Parmentier M, Sotin C, Travis B (1993) 3D convection at infinite Prandtl number in Cartesian geometry—a benchmark comparison. Geophys Astrophys Fluid Dyn 75:39–59

Čadek O, van den Berg AP (1998) Radial profiles of temperature and viscosity in the Earth's mantle inferred from the geoid and lateral seismic structure. Earth Planet Sci Lett 164:607–615

Crough ST (1978) Thermal origin of mid-plate hot-spot swells. Geophys J R Astron Soc 55:451–469

Cserepes L (1993) Effect of depth-dependent viscosity on the pattern of mantle convection. Geophys Res Lett 20:2091–2094

Cserepes L, Christensen UR, Ribe NM (2000) Geoid height versus topography for a plume model of the Hawaiian swell. Earth Planet Sci Lett 178:29–38

Davies GF (2000) Plates, plumes, mantle convection, and mantle evolution. In: Jackson I (ed) The Earth's mantle: composition, structure, and evolution. Cambridge University Press, Cambridge, pp 228–258

Detrick RS, Crough ST (1978) Island subsidence, hot spots, and lithosphere thinning. J Geophys Res 83:1236–1244

Galsa A, Cserepes L (2003) The number of hotspots in three-dimensional numerical models of mantle convection. Acta Geod Geophys Hung 38:103–109

Galsa A, Lenkey L (2007) Quantitative investigation of physical properties of mantle plumes in three-dimensional numerical models. Phys Fluids 19(11):116601

Ji Y, Nataf HC (1998) Detection of mantle plumes in the lower mantle by diffraction tomography: Hawaii. Earth Planet Sci Lett 159:99–115

Kiefer WS, Hager BH (1992) Geoid anomalies and dynamic topography from convection in cylindricaé geometry: applications to mantle plumes on Earth and Venus. Geophys J Int 108:198–214

King SD (1997) Geoid and topographic swells over temperature-dependent thermal plumes in spherical-axisymmetric geometry. Geophys Res Lett 24:3093–3096

King SD, Masters G (1992) An inversion for radial viscosity structure using seismic tomography. Geophys Res Lett 19:1551–1554

Kuslits LB, Farkas MP, Galsa A (2014) Effect of temperature-dependent viscosity on mantle convection. Acta Geod Geophys 49:249–263

McNutt M (1988) Thermal and mechanical properties of the Cape Verde Rise. J Geophys Res 93:2156–2202

Mitrovica JX, Forte AM (1997) Radial profile of mantle viscosity: results from the joint inversion of convection and postglacial rebound observables. J Geophys Res 102:2751–2759

Monnereau M, Cazenave A (1990) Depth and geoid anomalies over oceanic hotspot swells: a global survey. J Geophys Res 95:15429–15438

Montelli R, Nolet G, Dahlen FA, Masters G, Engdahl ER, Hung S (2004) Finite-frequency tomography reveals a variety of plumes in the mantle. Science 303:338–343

Montelli R, Nolet G, Dahlen FA, Masters G (2006) A catalogue of deep mantle plumes: new results from finite-frequency tomography. Geochem Geophys Geosyst 7:Q11007. doi:10.1029/2006GC001248

Morgan WJ (1971) Convection plumes in the lower mantle. Nature 230:42–43

Robinson EM, Parsons B (1988) Effect of a shallow low-viscosity zone on the formation of midplate swells. J Geophys Res 93:3144–3156

Sandwell DT, Mackenzie KR (1989) Geoid height versus topography for oceanic plateaus and swells. J Geophys Res 94:7403–7418

Shahraki M, Schmeling H (2012) Plume-induced geoid anomalies from 2D axi-symmetric temperature- and pressure-dependent mantle convection models. J Geodyn 59–60:193–206

Su W-J, Woodward RL, Dziewonski AM (1992) Deep origin of mid-ocean-ridge seismic velocity anomalies. Nature 360:149–152

Süle B (2005) The structure and the surface manifestation of mantle plumes in depth-dependent three-dimensional models. Acta Geod Geophys Hung 40(1):89–104

Tackley PJ (1996) Effects of strongly variable viscosity on three-dimensional compressible convection in planetary mantels. Geophys Res 101:3311–3332

Tackley PJ (2000a) Self-consistent generation of tectonic plates in time-dependent, three-dimensional mantle convection simulations. Geochem Geophys Geosyst 1:1021. doi:10.1029/2000GC000036

Tackley PJ (2000b) Self-consistent generation of tectonic plates in time-dependent, three-dimensional mantle convection simulations, 2. Strain weakening and asthenosphere. Geochem Geophys Geosyst 1:1026. doi:10.1029/2000GC000043

Woodhouse JH, Dziewonski AM (1984) Mapping the upper mantle: Three dimensional modelling of earth structure by inversion of seismic waveforms. J Geophys Res 89:5953–5986

Wolfe CJ, Bjarnason IT, VanDecar JC, Salamon SC (1997) Seismic structure of the Iceland mantle plume. Nature 385:245